Time-dependent density-functional theory of high-order harmonic generation from noble-gas atoms driven by orthogonally polarized two-color laser fields

Mitsuko Murakami [1,*] Oleg Korobkin [2] and Guo-Ping Zhang[1]
[1]*Department of Physics, Indiana State University, Terre Haute, Indiana 47809, USA*
[2]*Los Alamos National Laboratory, CCS-7, Los Alamos, New Mexico 87544, USA*

An orthogonally polarized two-color (OTC) field of frequency ratio 1 : 2 is known to generate both odd and even harmonic spectra in the mutually orthogonal directions of the fundamental and the second-harmonic fields, respectively. Recollision angles of an ionized electron driven back to its parent ion by an OTC field are inferred from the intensity ratio of odd and even harmonics, where the relative phase delays between the two-color fields can be used in time-resolved measurements on a subcycle time scale. In this work, we present the *ab initio*, many-electron calculation of time-resolved recollision angles of noble-gas atoms driven by an OTC field, based on the time-dependent density-functional theory. Our results agree well with experimental data by Shafir *et al.* in Nat. Phys. **5**, 412 (2009) of helium atom and New J. Phys. **12**, 073032 (2010) of neon atom.

I. INTRODUCTION

Photoionization of atoms driven by a linearly polarized laser field has been extensively studied in the past because it induces a wealth of interesting phenomena such as high-order harmonic generation (HHG) and above-threshold ionization. In the past decade, a new type of driving laser field, namely, an orthogonally polarized two-color (OTC) field, has successfully been applied to angle- and time-resolved measurement of noble-gas atoms; e.g., tomographic imaging of atomic orbitals [1], determination of ionization and recombination times of photoionized electrons [2], or stroboscopic measurements of photoelectron momentum distributions (PMDs) [3–5]. In these measurements, a second-harmonic field which is orthogonal to a fundamental field causes a transverse offset to the electron motion. The resulting electron trajectory can be a figure-8 shape or a boomerang shape, depending on the timing of ionization, which can be controlled by the relative phase delay between the two-color fields [6,7]. Just as in a linearly polarized field, an ionized electron releases its excess energy gained while being accelerated by an OTC field as high-order harmonic radiation upon recolliding with its parent ion. For the case of an OTC field whose frequency ratio is 1 : 2, both odd and even harmonics are generated in the mutually orthogonal directions of the fundamental and the second-harmonic fields, respectively, whereas the frequency ratio of 1 : 3 yields only odd harmonics which are elliptically polarized [8]. Note that the production of even harmonics from atoms driven by an OTC field is not due to broken inversion symmetry of the system [9] but due to two-color mixing [10]. Electron wave packets that are emitted in different quarter-cycles of the fundamental field appear in different quadrants of a PMD when driven by an OTC laser, which facilitates the analysis of their interference patterns [11,12].

Theoretically, the OTC field poses two unprecedented problems compared to the linearly polarized field. First is the loss of azimuthal symmetry, which leads to a fully three-dimensional (3D) problem. Secondly, the presence of an orthogonal field substantiates the need for a many-electron theory for the following reason. When driven by a linearly polarized laser field, the valence electrons in a *p*-shell ionize mostly from the $m = 0$ orbital that is oriented in parallel with the laser polarization axis, so that one can adopt the single active electron (SAE) approximation [13]. When another field is added perpendicular to the principal axis, however, *p*-shell electrons from the other two degenerate orbitals ($m = \pm 1$) can also ionize and contribute to high-order harmonic spectra, which makes the SAE approximation questionable. A numerically tractable approach in this case is to use time-dependent density-functional theory (TDDFT), which is based on a set of single-electron Kohn-Sham equations rather than a many-electron Schrödinger equation to describe the system [14]. Examples of different approaches to the 3D strong-field calculation include strong field approximation (SFA) [15], time-dependent Schrödinger equation (TDSE) [16–20], analytical *R*-matrix theory [21], quantum trajectory Monte Carlo method (QTMC) [11], and the Coulomb-corrected SFA [22]. To the best of our knowledge, however, many-electron calculation with an OTC field beyond the SAE approximation has not been reported. We have developed the numerical scheme to solve the 3D-TDSE for the hydrogen (H) atom driven by an OTC field based on the generalized pseudospectral (GPS) method in Ref. [18]. The question we would like to address in the present work is how to solve the 3D Kohn-Sham equations using the GPS method for many-electron atoms driven by an OTC field.

The paper is organized as follows. In Sec. II, we describe the numerical scheme for our TDDFT calculation. Then,

*Mitsuko.Murakami@indstate.edu

we present the high-order harmonic spectra of helium (He) and neon (Ne) atoms in Sec. III and compare them with experimental data in Refs. [1,23]. Our calculations are in good agreement with their experiments, showing the power of the TDDFT approach to HHG driven by an OTC field. Conclusion is given in Sec. IV. Atomic units ($e = m_e = \hbar = 1$) are used throughout, unless specified otherwise.

II. METHODS

A. Time-dependent Kohn-Sham equations

We solve the time-dependent Kohn-Sham equation in the length gauge, given by

$$i\frac{\partial}{\partial t}\psi_{i\sigma}(\mathbf{r}, t) = \mathcal{H}(\mathbf{r}, t)\,\psi_{i\sigma}(\mathbf{r}, t), \tag{1}$$

where $i = 1, 2, \ldots, N_\sigma$ ranges over occupied atomic orbitals, $\sigma \in \{\uparrow, \downarrow\}$ specifies the z component of the electron spin $s_z = \pm 1/2$, and

$$\mathcal{H}(\mathbf{r}, t) = \frac{-1}{2}\nabla^2 - \frac{Z}{r} + v_\sigma^{\mathrm{KS}}[n_\uparrow, n_\downarrow](\mathbf{r}, t) + V(\mathbf{r}, t), \tag{2}$$

in which Z is the atomic number of an atom, and $V(\mathbf{r}, t)$ is an external potential due to a driving laser field. The electron-electron interaction is contained in the Kohn-Sham potential $v_\sigma^{\mathrm{KS}}[n_\uparrow, n_\downarrow]$, which is a functional of the spin electron density:

$$n_\sigma(\mathbf{r}, t) = \sum_{i=1}^{N_\sigma} n_{i\sigma}(\mathbf{r}, t) = \sum_{i=1}^{N_\sigma} g_{i\sigma} |\psi_{i\sigma}(\mathbf{r}, t)|^2, \tag{3}$$

where $g_{i\sigma}$ is the occupation number of a state $\psi_{i\sigma}$, such that

$$\sum_\sigma \sum_{i=1}^{N_\sigma} g_{i\sigma} = Z. \tag{4}$$

In the limit of dipole approximation, the external laser potential is

$$V(\mathbf{r}, t) = \mathbf{r} \cdot \mathbf{E}(t), \tag{5}$$

where $\mathbf{E}(t)$ is the OTC laser field, defined by [15,17]

$$\mathbf{E}(t) = E_0(t)[\cos(\omega_0 t)\hat{\mathbf{z}} + \varepsilon\,\cos(2\omega_0 t + \beta)\hat{\mathbf{x}}], \tag{6}$$

in which β and ε are the phase delay and the field-strength ratio, respectively, between the fundamental and the secondary fields, and $E_0(t)$ is an envelope function centered around $t = 0$, given by

$$E_0(t) = \sqrt{I_0} \cos^2\left(\frac{\omega_0 t}{2n}\right), \tag{7}$$

with n being the number of cycles per pulse. Accordingly, Eq. (5) becomes

$$V(\mathbf{r}, t) = E_0(t)\, r[\cos\theta\,\cos(\omega_0 t)$$
$$+ \varepsilon\,\sin\theta\,\cos\phi\,\cos(2\omega_0 t + \beta)]. \tag{8}$$

The ϕ dependence in Eq. (8) breaks the azimuthal symmetry of the system, so the magnetic quantum number is no longer a conserved quantity. This means that the wave function $\psi_{i\sigma}(\mathbf{r}, t)$ for each orbital becomes fully asymmetrical and needs to be evolved as a 3D quantity when the OTC field turns on. This is a particular challenge with orthogonally

polarized laser fields and also with an elliptically polarized laser field [18]. For a linearly polarized laser field, whether monochromatic or not, the azimuthal symmetry is conserved, so that the problem is essentially two dimensional (2D) [13].

Our 2D-TDDFT calculations with noble-gas atoms in Ref. [13] showed that, when driven by a linearly polarized, near-infrared laser field, the valence electron in the p shell ionizes mostly from the $m = 0$ orbital that is oriented in parallel with the laser polarization axis, so that one could adopt the single active electron (SAE) approximation. With an OTC field, however, p-shell electrons from the other two degenerate orbitals ($m = \pm 1$) can also contribute to high-order harmonic spectra, so it is necessary to incorporate many electrons into calculation. The numerical scheme to solve the 3D-TDSE for the H atom driven by an OTC field based on the generalized pseudospectral method is described in Ref. [18]. The remaining question is therefore how to calculate the 3D Kohn-Sham potential $v_\sigma^{\mathrm{KS}}[n_\uparrow, n_\downarrow]$ in each time step for many-electron atoms.

B. Time-dependent Hartree potential

In general, the KS potential in Eq. (2) consists of two parts, namely,

$$v_\sigma^{\mathrm{KS}}[n_\uparrow, n_\downarrow](\mathbf{r}, t) = V_{\mathrm{H}}[n](\mathbf{r}, t) + v_\sigma^{\mathrm{xc}}[n_\uparrow, n_\downarrow](\mathbf{r}, t), \tag{9}$$

where V_{H} is the Hartree potential

$$V_{\mathrm{H}}[n](\mathbf{r}, t) = \iiint \frac{n(\mathbf{r}', t)}{|\mathbf{r} - \mathbf{r}'|}d^3\mathbf{r}', \tag{10}$$

which is a functional of the total electron density

$$n(\mathbf{r}, t) = \sum_\sigma n_\sigma(\mathbf{r}, t). \tag{11}$$

The second term $v_\sigma^{\mathrm{xc}}[n_\uparrow, n_\downarrow]$ in Eq. (9) is the exchange-correlation potential, which shall be discussed in the next section.

To find the 3D time-dependent Hartree potential (10), we use the Laplace expansion of an inverse distance, given by [24]

$$\frac{1}{|\mathbf{r} - \mathbf{r}'|} = \sum_{\ell, m} \frac{4\pi}{2\ell + 1}\left(\frac{r_<^\ell}{r_>^{\ell+1}}\right)Y_{\ell m}^*(\theta', \phi')Y_{\ell m}(\theta, \phi), \tag{12}$$

where $r_<$ (or $r_>$) represents the lesser (or greater) of $|\mathbf{r}|$ and $|\mathbf{r}'|$, and $Y_{\ell m}(\theta, \phi)$ are the spherical harmonics. Moreover, we expand the electron density with spherical harmonics, such that

$$n(\mathbf{r}, t) = \sum_{\ell, m} n_{\ell m}(r, t)Y_{\ell m}(\theta, \phi), \tag{13}$$

where

$$n_{\ell m}(r, t) = \iint d\Omega\, n(\mathbf{r}, t)Y_{\ell m}^*(\theta, \phi). \tag{14}$$

Then, Eq. (10) becomes

$$V_{\mathrm{H}}[n](\mathbf{r}, t) = \sum_{\ell, m} \frac{4\pi}{2\ell + 1}\left[r^\ell p_{\ell m}(r, t) + \frac{q_{\ell m}(r, t)}{r^{\ell+1}}\right]Y_{\ell m}(\theta, \phi), \tag{15}$$

where

$$p_{\ell m}(r, t) = \int_r^\infty \frac{n_{\ell m}(r', t)}{r'^{\ell+1}} r'^2 dr' \tag{16}$$

and

$$q_{\ell m}(r, t) = \int_0^r r'^\ell n_{\ell m}(r', t) r'^2 dr'. \tag{17}$$

In this work, we let $\ell_{\max} = 31$ (and $|m| \leqslant \ell_{\max}$), which is sufficient for the driving laser intensity we use ($I_0 = 1.8 \times 10^{14}$ W/cm^2). The radial coordinate is discretized using 250 Legendre-Lobatto collocation points which are denser near the origin, as described in Ref. [25].

C. Local spin-density approximation with a self-interaction correction

At the heart of TDDFT is the assumption that there exists a noninteracting system described by a set of Kohn-Sham equations (1) that possesses the same electron density as the interacting system described by the solution Ψ of the many-electron TDSE [26,27], i.e.,

$$n(\mathbf{r}, t) = N \iiint \cdots \iiint |\Psi(\mathbf{r}, \mathbf{r}_2, \cdots, \mathbf{r}_N)|^2 \, d^3\mathbf{r}_2 \cdots d^3\mathbf{r}_N. \tag{18}$$

Then, TDDFT is exact as long as the exchange-correlation potential $v_{\mathrm{xc}}^\sigma[n_\uparrow, n_\downarrow]$ in Eq. (9) is exact, but in practice one needs to approximate it. In the present work, we employ the local density approximation with a self-interaction correction (LDA-SIC), given by [28]

$$v_\sigma^{\mathrm{xc}}[n_\uparrow, n_\downarrow](\mathbf{r}, t) \simeq V_\sigma^{\mathrm{LDA}}[n_\sigma](\mathbf{r}, t) - V_\sigma^{\mathrm{SIC}}[n_{i\sigma}](\mathbf{r}, t), \tag{19}$$

where

$$V_\sigma^{\mathrm{LDA}}[n_\sigma](\mathbf{r}, t) = -\left(\frac{6}{\pi} n_\sigma(\mathbf{r}, t)\right)^{1/3} \tag{20}$$

and

$$V_\sigma^{\mathrm{SIC}}[n_{i\sigma}](\mathbf{r}, t) = V_\sigma^{\mathrm{SI}}(\mathbf{r}, t) + \frac{1}{n_\sigma(\mathbf{r}, t)} \sum_{i=1}^{N_\sigma}{}' n_{i\sigma}(\mathbf{r}, t) v_{i\sigma}(t). \tag{21}$$

In the last expression, $V_\sigma^{\mathrm{SI}}[n_{i\sigma}](\mathbf{r}, t)$ is the self-interaction potential given by

$$V_\sigma^{\mathrm{SI}}[n_{i\sigma}](\mathbf{r}, t) = \frac{1}{n_\sigma(\mathbf{r}, t)} \sum_{i=1}^{N_\sigma} n_{i\sigma}(\mathbf{r}, t) w_{i\sigma}(\mathbf{r}, t), \tag{22}$$

with

$$w_{i\sigma}(\mathbf{r}, t) = V_{\mathrm{H}}[n_{i\sigma}](\mathbf{r}, t) - V_\sigma^{\mathrm{LDA}}[n_{i\sigma}](\mathbf{r}, t). \tag{23}$$

Moreover, $v_{i\sigma}(t) \equiv \langle V_{i\sigma}^{\mathrm{SIC}}(t)\rangle - \langle w_{i\sigma}(t)\rangle$, where

$$\langle V_{i\sigma}^{\mathrm{SIC}}(t)\rangle = \iiint V_\sigma^{\mathrm{SIC}}[n_{i\sigma}](\mathbf{r}, t) n_{i\sigma}(\mathbf{r}, t) \, d^3\mathbf{r}, \tag{24}$$

and

$$\langle w_{i\sigma}(t)\rangle = \iiint w_{i\sigma}(\mathbf{r}, t) n_{i\sigma}(\mathbf{r}, t) \, d^3\mathbf{r}. \tag{25}$$

The asymptotic condition, where $V_\sigma^{\mathrm{SIC}} \to 0$ as $r \to \infty$, requires that $v_{i\sigma} = 0$ for the highest-occupied atomic orbitals

(HOAOs), and thus the primed summation $\sum'$ in Eq. (21) denotes a summation over all orbitals except for the HOAOs [29]. In practice, we calculate $v_{i\sigma}(t)$ noniteratively as [14]

$$v_{i\sigma}(t) = \sum_{j=1}^{N_\sigma}{}' [\mathbf{A}_\sigma^{-1}(t)]_{ij} [\langle V_{j\sigma}^{\mathrm{SI}}(t)\rangle - \langle w_{j\sigma}(t)\rangle], \tag{26}$$

where

$$[\mathbf{A}_\sigma(t)]_{ij} = \delta_{ij} - \iiint \frac{n_{i\sigma}(\mathbf{r}, t) n_{j\sigma}(\mathbf{r}, t)}{n_\sigma(\mathbf{r}, t)} d^3\mathbf{r} \tag{27}$$

and

$$\langle V_{j\sigma}^{\mathrm{SI}}(t)\rangle = \iiint V_\sigma^{\mathrm{SI}}[n_{i\sigma}](\mathbf{r}, t) n_{j\sigma}(\mathbf{r}, t) d^3\mathbf{r}. \tag{28}$$

Integrations involved in the calculation of a SIC term are straightforward because they depend only on a single coordinate $\mathbf{r}$, unlike the Hartree potential (10) discussed in the previous section.

The LDA-SIC approximation is free from spin-orbit coupling, so that electrons with opposite spins do not interact. For noble-gas atoms in particular, the number of linearly independent Kohn-Sham equations to be solved is therefore $Z/2$. The total density can then be found by multiplying the spin-up (or -down) electron density by 2. We have validated our implementation of the LDA-SIC approximation in Ref. [30] where the LDA-SIC ground-state energies of atoms for $Z \leqslant 18$ are compared with other various approximations. The LDA-SIC orbital energy of each Kohn-Sham wave function for He and Ne atoms in particular is given in Ref. [13], whose discrepancy from experimentally determined binding energy is within 8%.

D. Time evolution scheme

In the GPS method for an atom, the single-electron wave function is expanded by using spherical harmonics $Y_{\ell m}(\theta, \phi)$ as [25]

$$\psi_{i\sigma}(\mathbf{r}, t) = \sum_{\ell, m} \frac{R_{i\sigma}^{\ell m}(r, t)}{r} Y_{\ell m}(\theta, \phi), \tag{29}$$

where $\ell = 0, 1, 2, \ldots, \ell_{\max}$ and $|m| \leqslant \ell$. For the time evolution of Kohn-Sham wave function $\psi_{i\sigma}(\mathbf{r}, t)$, the Hamiltonian operator (2) is split into $\mathcal{H}_\ell^0(r) + U(\mathbf{r}, t)$, where $\mathcal{H}_\ell^0(r)$ is the stationary-state Hamiltonian given by [28]

$$\mathcal{H}_\ell^0(r) = \frac{-1}{2} \frac{\partial^2}{\partial r^2} + \frac{\ell(\ell+1)}{2r^2} - \frac{Z}{r} + v_\sigma^{\mathrm{KS}}[\bar{n}_{i\sigma}](r), \tag{30}$$

which is diagonal in each ℓ. The last term is the orbital-averaged Kohn-Sham potential [13]

$$v_\sigma^{\mathrm{KS}}[\bar{n}_{i\sigma}](r) = V_{\mathrm{H}}[\bar{n}](r, t_i) + V_\sigma^{\mathrm{LDA}}[\bar{n}_\sigma](r, t_i) - V_\sigma^{\mathrm{SIC}}[\bar{n}_{i\sigma}](r, t_i), \tag{31}$$

where $\bar{n}(r) = \sum_\sigma \bar{n}_\sigma(r)$ and $\bar{n}_\sigma(r) = \sum_{i=1}^{N_\sigma} \bar{n}_{i\sigma}(r)$, with

$$\bar{n}_{i\sigma}(r) = \frac{|R_{i\sigma}^{(\ell_i m_i)}(r, t_i)|^2}{4\pi r^2}, \tag{32}$$

and $t = t_i$ is the initial time before the laser field turns on. Note that ℓ_i and m_i in Eq. (32) are not summation indices but specific to each ith orbital, and thus it is enclosed in

parentheses. On the other hand, the time-dependent part of the Hamiltonian is fully 3D and given by [31]

$$U(\mathbf{r}, t) = v_\sigma^{\text{KS}}[n_\uparrow, n_\downarrow](\mathbf{r}, t) - v_\sigma^{\text{KS}}[\bar{n}_{i\sigma}](r) + V(\mathbf{r}, t), \quad (33)$$

where

$$v_\sigma^{\text{KS}}[n_\uparrow, n_\downarrow](\mathbf{r}, t) = V_{\text{H}}(\mathbf{r}, t) + V_\sigma^{\text{LDA}}[n_\sigma](\mathbf{r}, t) \\ - V_\sigma^{\text{SIC}}[n_{i\sigma}](\mathbf{r}, t). \quad (34)$$

Then, the Kohn-Sham wave function is evolved as [18]

$$\psi_{i\sigma}(\mathbf{r}, t + \Delta t) \simeq e^{-i\mathcal{H}_\ell^0(r)\Delta t/2} \mathcal{S}^{-1}(\ell, m) e^{-iU(\mathbf{r}, t+\Delta/2)\Delta t} \\ \times \mathcal{S}(\theta, \phi) e^{-i\mathcal{H}_0(\ell)\Delta t/2} \psi_{i\sigma}(\mathbf{r}, t), \quad (35)$$

where $\mathcal{S}$ denotes the spherical harmonic transform [32], i.e.,

$$\mathcal{S}\{\varphi_\ell^m(r, t)\}(\theta, \phi) = \frac{1}{\sqrt{2\pi}} \sum_{\ell, m} e^{im\phi} \\ \times \sqrt{\frac{(2\ell + 1)(\ell - m)!}{2(\ell + m)!}} P_\ell^m(\cos\theta) \, \varphi_\ell^m(r, t) \\ = \varphi(r, \theta, \phi, t), \quad (36)$$

which provides the change in representation: $(\ell, m) \to (\theta, \phi)$ for any function φ in the spherical coordinates. The TDDFT calculation with nonspherical atomic orbitals is less stable and requires smaller time steps than with spherical orbitals. In this work, we let $\Delta t = 0.2$ a.u. for a He atom and $\Delta t = 0.01$ a.u. for a Ne atom to ensure the stability during their time evolution for 20 optical cycles.

Moreover, to eliminate the reflection from the boundary during the time evolution, we split the wave function at a given time t as

$$\psi(\mathbf{r}, t) = f(r)\psi(\mathbf{r}, t) + [1 - f(r)]\psi(\mathbf{r}, t) \\ = \psi_{(\text{in})}(\mathbf{r}, t) + \psi_{(\text{out})}(\mathbf{r}, t), \quad (37)$$

where $f(r)$ is an absorbing function that is 1 in the inner region ($0 \leqslant r \leqslant R_b$) and smoothly decreases to zero in the outer region ($R_b < r < r_{\max}$). For the evaluation of high-order harmonic spectra, only the inner wave function is necessary. In this work, we let $r_{\max} = 5\alpha_0$, where $\alpha_0 = E_0^2/\omega_0^2 = 22.1$ a.u. is the classical oscillator radius of a driving laser field, and $R_b = 1.1273\alpha_0$, which is known to minimize the effect of long paths in high-order harmonic spectra [33].

E. Evaluation of dipole spectra

In order to obtain the dipole spectra, we need to find the expectation values of the acceleration vector $\mathbf{a} = a_z\hat{\mathbf{z}} + a_x\hat{\mathbf{x}}$ in each time step. From Ehrenfest's theorem, its components are given by

$$\langle a_z \rangle = - \sum_\sigma \sum_{i=1}^{N_\sigma} \langle \psi_{i\sigma} | \nabla U_{\text{ext}}(\mathbf{r}) \cdot \hat{\mathbf{z}} | \psi_{i\sigma} \rangle \quad (38)$$

and

$$\langle a_x \rangle = - \sum_\sigma \sum_{i=1}^{N_\sigma} \langle \psi_{i\sigma} | \nabla U_{\text{ext}}(\mathbf{r}) \cdot \hat{\mathbf{x}} | \psi_{i\sigma} \rangle. \quad (39)$$

The external potential is

$$U_{\text{ext}}(\mathbf{r}) = -\frac{Z}{r} + v_\sigma^{\text{KS}}[n_\uparrow, n_\downarrow](\mathbf{r}, t). \quad (40)$$

We do not need to include the laser potential $V(\mathbf{r}, t)$ in the above expression, because it only contributes to the fundamental harmonic yield and not to higher-order harmonics.

The zero-force theorem of TDDFT [34] states that the Kohn-Sham potential $v_\sigma^{\text{KS}}[n_\uparrow, n_\downarrow](\mathbf{r}, t)$, which accounts for the electron-electron interaction, does not contribute to the dipole acceleration only if it is exact, i.e., if the spin electron densities given by (3) sum up to the total electron density (18) given by the many-electron TDSE. Although the exchange-correlation potential we use is approximate, we shall assume that the zero-force theorem holds when evaluating the dipole acceleration. It then follows that (whose proof is given in the Appendix)

$$\langle a_z(t) \rangle = -2Z \sum_\sigma \sum_{i=1}^{N_\sigma} \sum_{\ell, m} \\ \times \int dr \left(\frac{c_\ell^m}{r^2}\right) \text{Re}\left[R_{i\sigma}^{*\ell+1, m}(r, t) R_{i\sigma}^{\ell m}(r, t)\right], \quad (41)$$

where

$$c_\ell^m = \sqrt{\frac{(\ell + m + 1)(\ell - m + 1)}{(2\ell + 1)(2\ell + 3)}} \quad (42)$$

and

$$\langle a_x(t) \rangle = -Z \sum_\sigma \sum_{i=1}^{N_\sigma} \sum_{\ell, m} \int dr \left(\frac{1}{r^2}\right) \\ \times \text{Re}\left[\kappa_\ell^m R_{i\sigma}^{*\ell m}(r, t) R_{i\sigma}^{\ell+1, m+1}(r, t) \\ + \kappa_\ell^{-m} R_{i\sigma}^{*\ell m}(r, t) R_{i\sigma}^{\ell+1, m-1}(r, t)\right], \quad (43)$$

where

$$\kappa_\ell^m = \sqrt{\frac{(\ell + m + 1)(\ell + m + 2)}{(2\ell + 1)(2\ell + 3)}}. \quad (44)$$

In our previous publication of Ref. [18], these expressions for $\langle a_z(t) \rangle$ and $\langle a_x(t) \rangle$ were missing an overall factor of 2. The high-order harmonic spectra along the z or the x axis are found by taking the Fourier transforms of $\langle a_z(t) \rangle$ or $\langle a_x(t) \rangle$, respectively. That is,

$$D_{z,x}(\omega) = \frac{1}{t_f - f_i} \frac{1}{\omega^2} \int_{t_i}^{t_f} e^{-i\omega t} \langle a_{z,x}(t) \rangle dt, \quad (45)$$

where t_i and t_f are the beginning and the ending of the time evolution. Then, their square moduli $|D_z(\omega)|^2$ and $|D_x(\omega)|^2$ give the intensity of odd and even high-order harmonic spectra, respectively, in arbitrary units.

F. Recollision angles

Odd- and even-order harmonics generated by an OTC field are polarized exclusively along the fundamental and the secondary field vectors, respectively [15]. Therefore, the recollision angles of ionized electrons with the parent ion can

be inferred from harmonic spectra as [18]

$$|\theta_{\rm rec}(\omega)| = \arctan\left(\sqrt{\frac{|I_x(\omega)|}{|I_z(\omega)|}}\right), \qquad (46)$$

where $I_{z,x}(\omega) = |D_{z,x}(\omega)|^2$. Note that the adjacent harmonics are interpolated to obtain continuous spectra separately for even- and odd-order harmonics before taking their intensity ratio. Moreover, we can calculate the time-resolved recollision angles as

$$|\theta_{\rm rec}(\omega, t)| = \arctan\left(\sqrt{\frac{|G_x(\omega, t)|}{|G_z(\omega, t)|}}\right), \qquad (47)$$

where $G_{z,x}(t, \omega)$ is the Gabor transform of dipole accelerations, defined by [17]

$$G_{z,x}(t, \omega) = \left| \int e^{-i\omega t'} \langle a_{z,x}\rangle(t', \beta) E_G(t' - t) \, dt' \right|^2, \quad (48)$$

with

$$E_G(t) = \frac{\exp\left[-t^2/2\sigma_o{}^2\right]}{\sqrt{2\pi}\sigma_o}. \qquad (49)$$

The width of a sweeping function $E_G(t)$ is set to be $\sigma_o = (3\omega_0)^{-1}$ [35].

III. RESULTS

For high-order harmonic spectra presented in this section, the driving OTC laser (800+400 nm) has a duration of $n = 20$ optical cycles and a peak intensity of $I_0 = 1.8 \times 10^{14}$ W/cm^2 (i.e., $\omega_0 = 0.056961$ a.u. and $\sqrt{I_0} = 0.071714$ a.u.), to be consistent to the experiment in Ref. [23]. The field-strength ratio in Eq. (6) is set $\varepsilon = 1/2$, so that the intensity ratio between the fundamental field (800 nm) and the second harmonic field (400 nm) is 4:1, also consistent with Ref. [23].

In Fig. 1, we plot the ionization probability of Kohn-Sham orbitals in the L shell of a Ne atom during the time evolution driven by the OTC field for two two-color delays: $\beta = 0$ and $\pi/2$. They are evaluated as the electron density outside the radius $r = 10$ a.u. This figure illustrates the fact that the ionization probabilities of different orbitals are in the same order of magnitude when driven by the OTC field we use in this work, and therefore the SAE approximation may not be appropriate.

Figure 2 shows high-order harmonic spectra of the He atom, which are calculated with various phase delays β between the fundamental and the second harmonic fields of the OTC laser. The harmonic cutoff predicted by the cutoff law $I_p + 3.17U_p$ [36,37] is $38\omega_0$, where $I_p = 0.918$ a.u. and $U_p = E_0{}^2/4\omega_0{}^2 = 0.396$ a.u. are the ionization energy of the He atom and the ponderomotive energy of a driving laser field, respectively. The most important feature in these spectra is that the intensity of odd harmonics (D_z) is much stronger than the intensity of even harmonics (D_x) near and beyond the cutoff energy. The same behavior was reported in the He measurement of Ref. [1]. This is a characteristic of atoms whose valence orbitals are spherically symmetric, such as H and He [18,23]. According to Eq. (46), $D_z \gg D_x$ indicates small recollision angles for electron trajectory. Therefore,
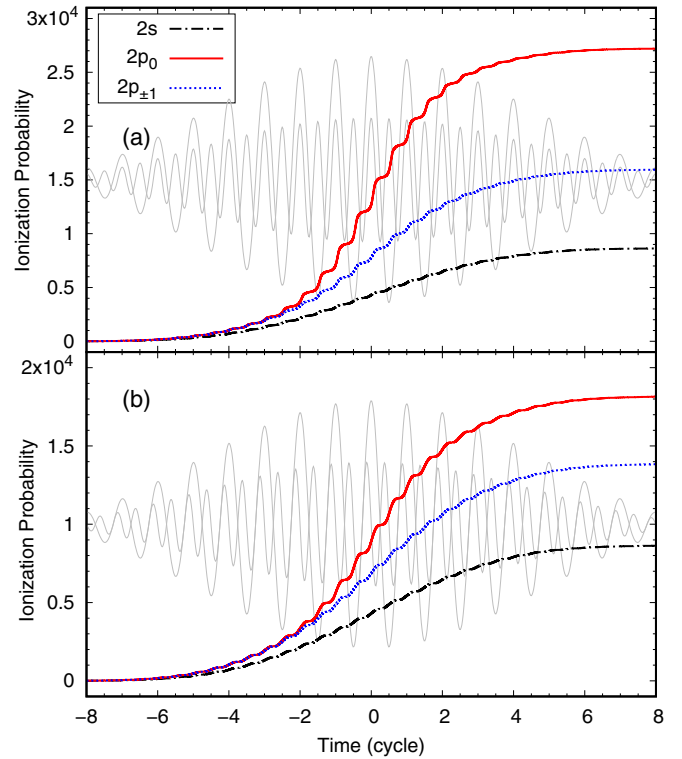

FIG. 1. Ionization probability of Kohn-Sham wave functions in the L shell of a Ne atom, driven by 20-cycle, mutually orthogonal two-color (800+400 nm) laser pulse of peak intensity $I_0 = 1.8 \times 10^{14}$ W/cm^2, when the relative phase delay between the two-color fields are (a) $\beta = 0$ and (b) $\beta = \pi/2$. Time is shown in one optical cycle of 800 nm laser, which corresponds to $2\pi/\omega_0 = 2.67$ fs. Also shown in the background is the laser field strengths of two-color fields in arbitrary units. The field strength of the fundamental field is set to be two times stronger than the second-harmonic field, so that their intensity ratio is 4 : 1 in accordance with Refs. [1,23].

Fig. 2 suggests that spherically symmetric atoms in an OTC field prefer small collision angles in order to attain higher frequency.

Another interesting observation in Fig. 2 is that harmonics in the plateau region are extremely well resolved when the relative delay between the two-color fields is $\beta = \pi/2$. This is a well-known effect in HHG driven by an OTC field [15]. When we study HHG driven by a linearly polarized laser field in the single-atom level (i.e., without macroscopic propagation effect), the plateau harmonics tend to appear noisy with no regularly spaced peaks because of the quantum interference between the two degenerate electron paths, often referred to as short and long quantum trajectories [37]. In HHG experiments, long-path harmonics, which are more divergent than the short, can be eliminated by adjusting the position of the noble-gas jet relative to the laser focus, which produces cleaner plateau harmonics similar to those in Fig. 2(c). The selection of electron trajectory in HHG calculations with a linearly polarized laser field is not possible unless we take the propagation effect of high-order harmonic fields through generating medium into consideration [38]. This makes the comparison between the experiment and the single-atom calculation with a linearly polarized laser somewhat difficult.
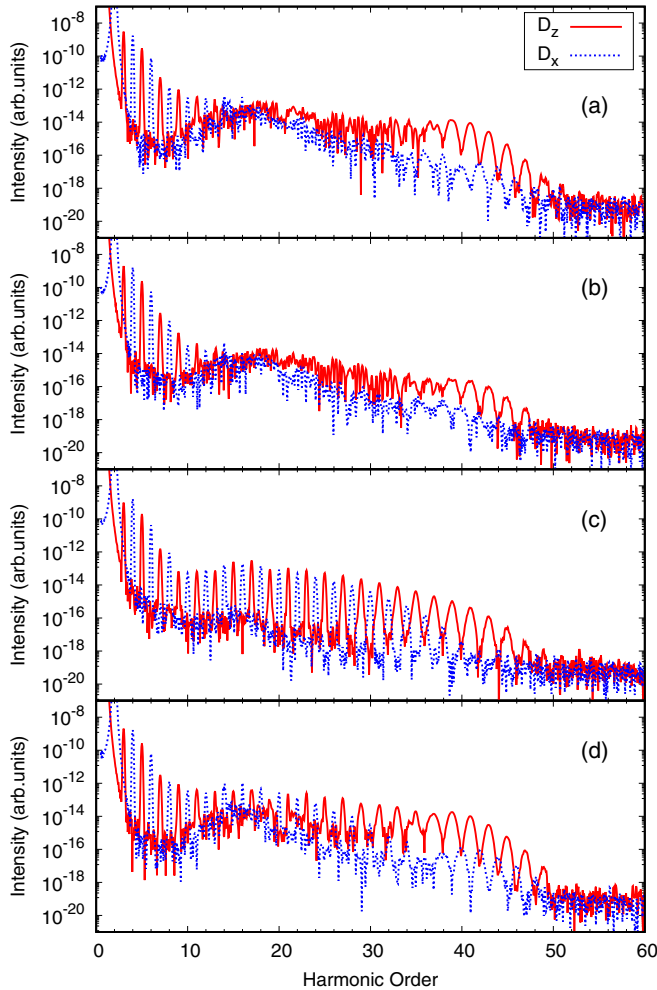
FIG. 2. High harmonic spectra of a He atom, driven by 20-cycle, orthogonally polarized two-color laser pulse with relative phase delays of (a) $\beta = 0$, (b) $\beta = \pi/4$, (c) $\beta = \pi/2$, and (d) $\beta = 3\pi/4$. The fundamental field (800 nm) along the z axis has a peak intensity of $I_0 = 1.8 \times 10^{14}$ W/cm^2, which is four times larger than the peak intensity of the second harmonic field (400 nm) along the x axis. Harmonic spectra in the plateau region (15–$38\omega_0$) does not show regularly spaced peaks in Figs. 2(a) and 2(b), due to the quantum interference between the two degenerate electron paths (long and short). On the other hand, regularly spaced peaks in the plateau harmonics of Fig. 3(c) is an evidence of nondegenerate electron paths.

For HHG driven by an OTC field, on the other hand, we can limit the relative strength of the long-path contribution in a single-atom level by simply changing the relative phase β between the two-color fields, regardless of the source atoms.

Figure 3 shows the high-order harmonic spectra of a Ne atom driven by the same OTC field as in Fig. 2. The cutoff order predicted by the cutoff law is $36\omega_0$ ($I_p = 0.808$ a.u. based on the LDA-SIC approximation). We find that the even harmonics (D_x) in Fig. 3 remain comparably strong with odd harmonics (D_z) near the cutoff, contrary to the trend we saw in Fig. 2. In fact, the intensity of even harmonics is much stronger than odd harmonics in the lower plateau region when $\beta = \pi/4$ in Fig. 3(b). Experimental data of Ne atoms in
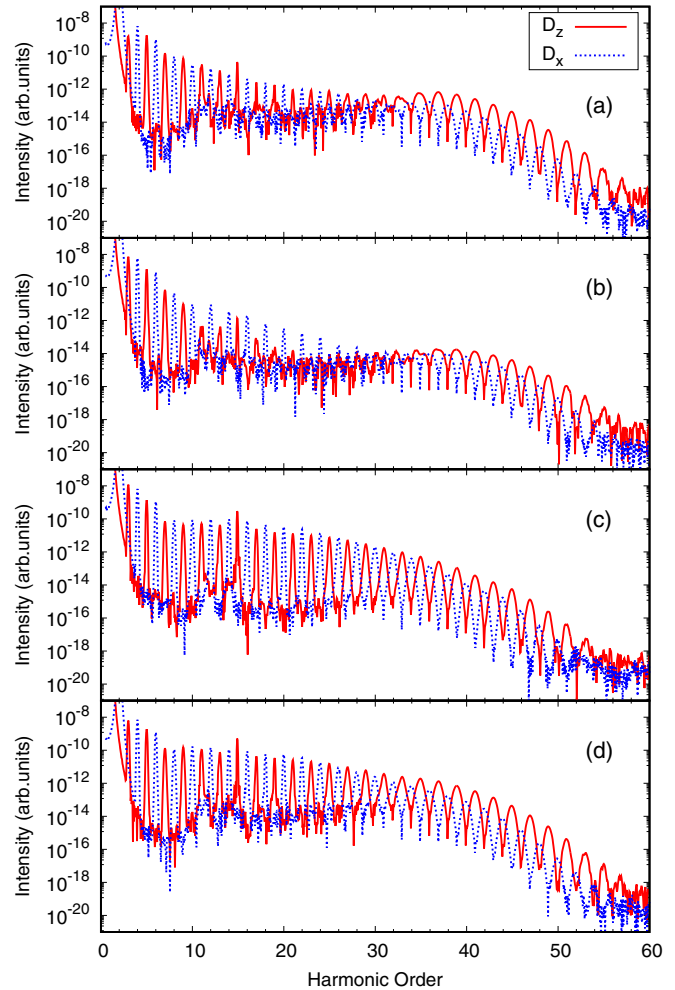

FIG. 3. Same as Fig. 2 but of a Ne atom. Unlike in Fig. 2, the even harmonics (D_x) have comparably strong intensity as the odd harmonics (D_z) near the cutoff ($36\omega_0$), indicating larger collision angles for upper-plateau harmonics generated from Ne than He.

Refs. [1,23] also exhibit the same behavior, i.e., their even harmonics are equally strong with odd harmonics in the cutoff region (29–$35\omega_0$), and they dominate over odd harmonics at low frequency. Authors then argued that these strikingly different trends between He and Ne reflect the symmetry of valence orbitals of parent ions seen by the free electron as they collide and produce high-order harmonic spectra. That is, electrons emitted from the $2p$ orbitals of Ne atoms tend to have larger recollision angles than those emitted from the $1s$ orbital of He atoms. This is reasonable because electron density of the p orbitals is sparse in between the three degenerate lobes ($m = 0, \pm 1$), through which the returning electron may preferentially find its passage to avoid electron-electron repulsion.

To study this effect further, we plot the recollision angles as a function of two-color delays β, derived from Eq. (46) in Figs. 4 and 5 for He and Ne atoms, respectively. In Refs. [1,23], recollision angles were evaluated from the experimental harmonic intensities for He and Ne atoms. Note that measurements in Refs. [1,23] only covered the range of phase delays between $\beta = 0$ and $\pi/2$ (which corresponds to
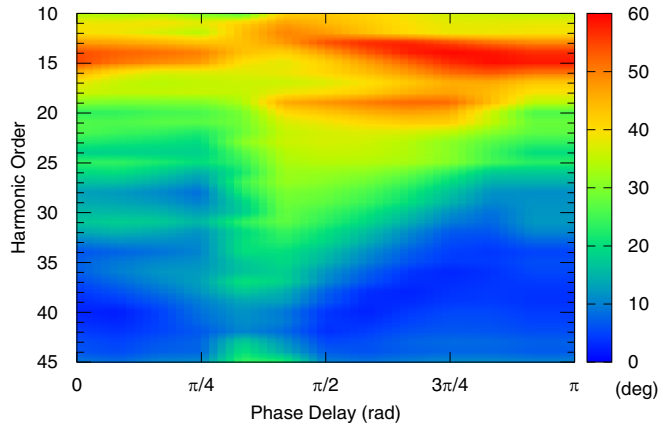
FIG. 4. Recollision angles of an ionized electron from the He atom, driven by 20-cycle, two-color (800 nm and 400 nm) mutually orthogonal laser pulse (of peak intensities $I_1 = 1.8 \times 10^{14}$ and $I_2 = 0.45 \times 10^{14}$ W/cm^2, respectively) as a function of relative phase delays β between the two-color fields, derived from Eq. (46). Recollision angles of lower plateau harmonics (20–$30\omega_0$) are $30°$–$40°$, whereas the upper plateau harmonics (30–$40\omega_0$) have smaller collision angles (below $20°$), which is in agreement with Ref. [1].

the quarter of an optical cycle or 0.667 fs), whereas our phase delays in Figs. 4 and 5 cover all the possible range ($0 \leqslant \beta < \pi$). The recollision angles in Figs. 4 and 5 agree with the results in Refs. [1,23] very well, showing the relevance of our TDDFT approach to the calculation of HHG driven by an OTC field. Specifically, for He, the recollision angles of lower plateau harmonics (20–$30\omega_0$) for experimentally measured range ($0 < \beta < \pi/2$) are $30°$–$40°$, whereas the upper plateau harmonics (30–$40\omega_0$) have smaller recollision angles (below $20°$), in agreement with Ref. [1]. On the other hand, the recollision angles of Ne for $0 < \beta < \pi/2$ are above $40°$ for all plateau harmonics (25–$35\omega_0$) except around $15\omega_0$, also in agreement with Ref. [23].

We have previously studied the time-resolved recollision angles for the H atom using Gabor transforms in Ref. [18]
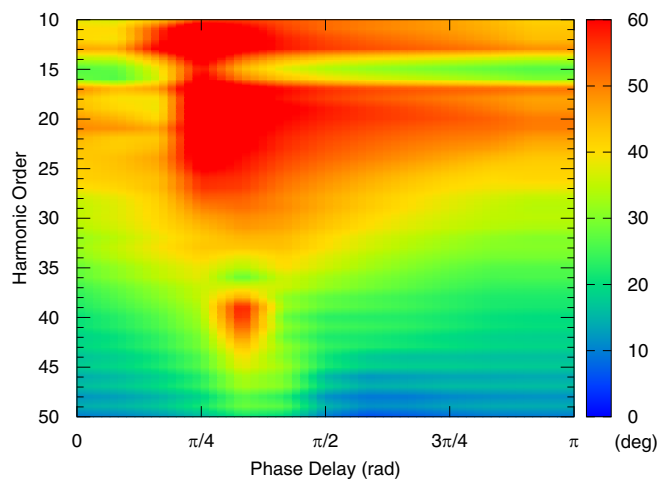
and found that the recollision angles of short-path harmonics are $20°$–$40°$ with respect to the fundamental laser axis. Assessment of recollision angles based on Gabor transforms allows better understanding of electron dynamics at subcycle time scale, particularly if it is combined with a proper choice of two-color phase delay β. In Figs. 6 and 7, we plot the time-resolved recollision angles of He and Ne atoms derived using Eq. (47) specifically from those dipole accelerations obtained with $\beta = \pi/2$, in order to select the short paths that dominate in experimental data. Also shown with dots in these figures is the return energy of a free electron moving in a linearly polarized laser field as a function of collision time, according to Newton's equation of motion: $\ddot{z} = -E_0(t)\cos(\omega_0 t)$ [18]. They follow a curved pattern which repeats every half of an optical cycle. Short-path solutions correspond to a set of points whose return energy is on the rising side of the curve.
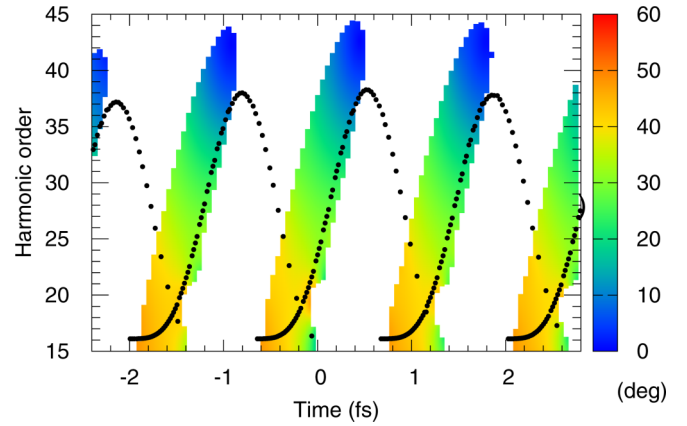

FIG. 6. Time-resolved recollision angle of an electron from the He atom, obtained by Gabor transforming the dipole acceleration for which the relative delay between the two-color laser fields is $\beta = \pi/2$. Also shown with dots is the return energy of a free electron moving in a linearly polarized laser field as a function of collision time, according to Newton's equation of motion.

FIG. 5. Same as Fig. 4 but for the Ne atom. Recollision angles in the plateau region (15–$36\omega_0$) are relatively large ($>30°$) compared to the results with He in Fig. 4, which is in agreement with Ref. [23].
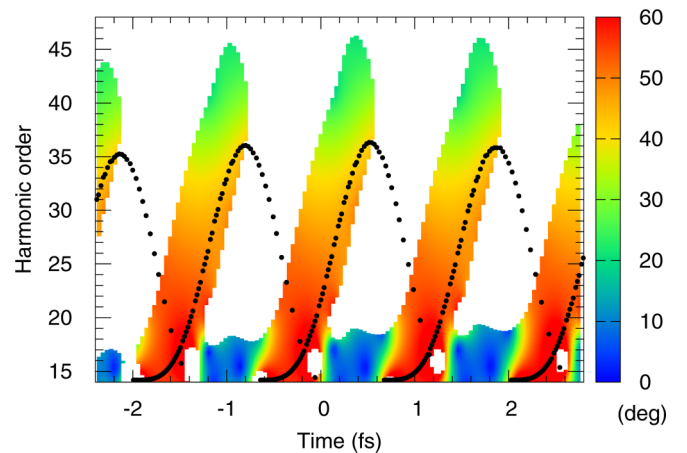

FIG. 7. Same as Fig. 6 but of the Ne atom. Agreement with the experimental data in Ref. [23] is even better than in Fig. 5 because of the two-color delay $\beta = \pi/2$ we use in the calculation of Fig. 6, which selects only the short-path recollisions which dominate in experiments.

We see that Gabor transforms appear exclusively along the short-path solutions of Newton's equation, confirming the successful path control by the two-color delay. From these figures, it is clear that electron motion, characterized by its recollision angles in this case, is periodic in every half of an optical cycle. For a heteronuclear diatomic molecule in an OTC field, this period would be a full optical cycle due to the broken inversion symmetry [39]. Focusing on the recollision angles in each half-cycle period in Figs. 6 and 7, one should notice that the agreement with Refs. [1,23] is even better than in Figs. 4 and 5; this is because we chose $\beta = \pi/2$ to select short-path trajectories while generating these plots, which made the results more consistent with the experiments.

IV. CONCLUSION

In this work, we presented the many-electron calculation of high-order harmonic generation (HHG) of helium and neon atoms driven by an orthogonally polarized two-color (OTC) field of frequency ratio 1 : 2. The intensity ratio between the odd and even high-order harmonics are used to determine the recollision angles of ionized electron with its parent ion. In order to avoid the quantum interference of degenerate electron paths in our calculation, we used the relative phase delay $\beta = \pi/2$ between the two-color fields to select short paths. Resulting dipole acceleration is then analyzed using Garbor transforms, which gives the time-resolved recollision angles measured in experiments in Refs. [1,23]. Our results are in excellent agreement with their data, validating the TDDFT approach to the HHG driven by an OTC laser. It should be emphasized that an OTC field not only breaks the azimuthal symmetry of the system but also demands many-electron theory beyond the single active electron approximation, in cases where the second-harmonic field perpendicular to the fundamental field makes the ionization rate of $m = \pm1$ orbitals in the p-shell comparable to the $m = 0$ orbital. We found that this is indeed true even though the peak intensity of the second-harmonic field is relatively weak compared to the fundamental field (4 : 1 in our calculation). We believe further studies with an OTC field could in principle reveal many-electron effects in high-order harmonic spectra or photoelectron momentum distributions of nonspherical atoms such as neon and argon, which would help finding the correct exchange-correlation potential in the Kohn-Sham equations and drive further development of TDDFT in the strong-field physics.

APPENDIX

Derivation of acceleration components

To derive Eqs. (41) and (43), we start with the z-component operator $\hat{\mathbf{a}}_z = -\partial_z \hat{U}_{\text{ext}}$, by writing it in spherical harmonics representation using the ket-bra notation:

$$\hat{\mathbf{a}}_z = -\sum_{\ell m} \left(\frac{\partial V}{\partial z}\right)^{(\ell m)} |\ell m\rangle \langle \ell m|.$$

Here, $V(r) := -Z/r$ is the spherically symmetric potential of the nucleus, and $|\ell m\rangle$ are spherical harmonics $Y_{\ell m}(\theta, \phi)$, defined as usual:

$$Y_{\ell m}(\theta, \phi) := \sqrt{\frac{(2\ell + 1)}{4\pi} \frac{(\ell - m)!}{(\ell + m)!}} \, P_\ell^m(\mu) \, e^{im\phi},$$

where $\mu := \cos\theta$ and $P_\ell^m(\mu)$ are associated Legendre polynomials. Using the chain rule for the derivative, the acceleration operator becomes

$$\hat{\mathbf{a}}_z = -\sum_{\ell m} \frac{\partial V}{\partial r}\left(\frac{\partial r}{\partial z}\right)^{(\ell m)} |\ell m\rangle \langle \ell m| = -\frac{\partial V}{\partial r} \sum_{\ell m} \mu \, |\ell m\rangle \langle \ell m|.$$

To get rid of μ in the sum, we can expand $|\ell m\rangle$ using the definition of spherical harmonics and apply a recurrence identity for the associated Legendre polynomials to the product $\mu P_\ell^m(\mu)$:

$$\hat{\mathbf{a}}_z = -\frac{\partial V}{\partial r} \sum_{\ell m} \mu Y_{\ell m}^*(\theta, \phi) Y_{\ell m}(\theta, \phi)$$

$$= -\frac{\partial V}{\partial r} \sum_{\ell m} \mu P_\ell^m(\mu) e^{-im\phi} P_\ell^m(\mu) e^{im\phi} \frac{(2\ell + 1)}{4\pi} \frac{(\ell - m)!}{(\ell + m)!}$$

$$= -\frac{\partial V}{\partial r} \sum_{\ell m} \left[\mu \, P_\ell^m(\mu)\right] P_\ell^m(\mu) \frac{(2\ell + 1)}{4\pi} \frac{(\ell - m)!}{(\ell + m)!}$$

$$= -\frac{\partial V}{\partial r} \sum_{\ell m} \left[\frac{(\ell - m + 1)P_{\ell+1}^m(\mu) + (\ell + m)P_{\ell-1}^m(\mu)}{2\ell + 1}\right]$$

$$\times P_\ell^m(\mu) \frac{(2\ell + 1)}{4\pi} \frac{(\ell - m)!}{(\ell + m)!}.$$

Now we can go back to the ket-bra notation by replacing

$$P_{\ell+1}^m P_\ell^m \rightarrow \frac{1}{2}|\ell + 1, m\rangle \langle \ell m| + \frac{1}{2}|\ell m\rangle \langle \ell + 1, m|,$$

$$P_{\ell-1}^m P_\ell^m \rightarrow \frac{1}{2}|\ell - 1, m\rangle \langle \ell m| + \frac{1}{2}|\ell m\rangle \langle \ell - 1, m|.$$

That is,

$$P_{\ell+1}^m P_\ell^m \frac{(\ell - m + 1)}{2\ell + 1} \frac{(2\ell + 1)}{4\pi} \frac{(\ell - m)!}{(\ell + m)!}$$

$$= \frac{1}{2}(|\ell + 1, m\rangle \langle \ell m| + |\ell m\rangle \langle \ell + 1, m|)$$

$$\times \sqrt{\frac{(\ell + 1 - m)(\ell + 1 + m)}{(2\ell + 1)(2\ell + 3)}},$$

$$P_{\ell-1}^m P_\ell^m \frac{(\ell+m)}{2\ell+1} \frac{(2\ell+1)}{4\pi} \frac{(\ell-m)!}{(\ell+m)!}$$

$$= \frac{1}{2}(|\ell-1,m\rangle\langle\ell m| + |\ell m\rangle\langle\ell-1,m|)$$

$$\times \sqrt{\frac{(\ell-m)(\ell+m)}{(2\ell-1)(2\ell+1)}}.$$

The expression for $\hat{\mathbf{a}}_z$ becomes

$$\hat{\mathbf{a}}_z = -\frac{\partial V}{\partial r} \sum_{\ell m}\left[\frac{c_{\ell-1}^m}{2}|\ell-1,m\rangle\langle\ell m| + \frac{c_\ell^m}{2}|\ell+1,m\rangle\langle\ell m|\right.$$
$$\left. + \frac{c_{\ell-1}^m}{2}|\ell m\rangle\langle\ell-1,m| + \frac{c_\ell^m}{2}|\ell m\rangle\langle\ell+1,m|\right], \quad \text{(A1)}$$

where

$$c_\ell^m := \sqrt{\frac{(\ell+m+1)(\ell-m+1)}{(2\ell+1)(2\ell+3)}}.$$

This can be further simplified if we collect similar terms after relabeling $\ell-1 \to \ell$ in the first and the third terms:

$$\hat{\mathbf{a}}_z = -\frac{\partial V}{\partial r}\sum_{\ell m} c_\ell^m(|\ell+1,m\rangle\langle\ell m| + |\ell m\rangle\langle\ell+1,m|).$$

(A2)

With this expression, a wave function $|\psi\rangle = 1/r \sum R_{\ell m}(r)|\ell m\rangle$ produces the expectation value

$$\langle\psi|\hat{\mathbf{a}}_z|\psi\rangle = -2\int\left(\frac{\partial V}{\partial r}\right)\sum_{\ell m} c_\ell^m \, \mathrm{Re}\big[R_{\ell+1,m}^*(r)R_{\ell m}(r)\big]dr,$$

(A3)

which after applying discretization produces Eq. (41).

To calculate the expectation value of $\hat{\mathbf{a}}_x$ we resort to the notion of reduced matrix elements $\langle\ell' \parallel \mathbf{a} \parallel \ell\rangle$, following Landau and Lifshitz [[40], Chap. 29]. z component of a polar vector such as $\mathbf{a}$ has nonzero matrix elements only for transitions which both conserve magnetic quantum number m and change total momentum quantum number ℓ by one. The general form of such matrix elements in terms of reduced matrix elements is

$$\langle\ell-1,m\,|\,\hat{\mathbf{a}}_z\,|\,\ell m\rangle = \sqrt{\frac{\ell^2-m^2}{\ell(2\ell-1)(2\ell+1)}}\langle\ell-1\parallel\mathbf{a}\parallel\ell\rangle.$$

(A4)

Comparing this to (A2), we can read out the reduced matrix element of the acceleration:

$$\langle\ell\parallel\mathbf{a}\parallel\ell-1\rangle = \langle\ell-1\parallel\mathbf{a}\parallel\ell\rangle = \frac{\partial V}{\partial r}\sqrt{\ell}. \quad \text{(A5)}$$

Matrix elements of the x component of a polar vector are nonzero only for those transitions in which both quantum numbers m and ℓ change by 1:

$$\langle\ell,m-1\,|\,\hat{\mathbf{a}}_x\,|\,\ell-1,m\rangle = \langle\ell-1,m\,|\,\hat{\mathbf{a}}_x\,|\,\ell,m-1\rangle$$

$$= \frac{1}{2}\sqrt{\frac{(\ell-m+1)(\ell-m)}{\ell(2\ell-1)(2\ell+1)}}\langle\ell\parallel\mathbf{a}\parallel\ell-1\rangle,$$

$$\langle\ell-1,m-1\,|\,\hat{\mathbf{a}}_x\,|\,\ell,m\rangle = \langle\ell,m\,|\,\hat{\mathbf{a}}_x\,|\,\ell-1,m-1\rangle$$

$$= \frac{1}{2}\sqrt{\frac{(\ell+m-1)(\ell+m)}{\ell(2\ell-1)(2\ell+1)}}\langle\ell-1\parallel\mathbf{a}\parallel\ell\rangle.$$

Substituting here the expression for the reduced matrix elements (A5), one obtains

$$\langle\ell,m-1\,|\,\hat{\mathbf{a}}_x\,|\,\ell-1,m\rangle = \langle\ell-1,m\,|\,\hat{\mathbf{a}}_x\,|\,\ell,m-1\rangle$$

$$= \kappa_{\ell-1}^{-m}\frac{1}{2}\left(\frac{\partial V}{\partial r}\right),$$

$$\langle\ell-1,m-1\,|\,\hat{\mathbf{a}}_x\,|\,\ell,m\rangle = \langle\ell,m\,|\,\hat{\mathbf{a}}_x\,|\,\ell-1,m-1\rangle$$

$$= \kappa_{\ell-1}^{m-1}\frac{1}{2}\left(\frac{\partial V}{\partial r}\right),$$

where

$$\kappa_\ell^m := \sqrt{\frac{(\ell+m+1)(\ell+m+2)}{(2\ell+1)(2\ell+3)}}.$$

The final expression for the expectation value of the x component is

$$\langle\psi|\hat{a}_x|\psi\rangle = -\int dr\left(\frac{\partial V}{\partial r}\right)$$

$$\times \sum_{\ell=0}^{\infty}\sum_{m=-\ell}^{\ell}\mathrm{Re}\big[\kappa_\ell^m R_{\ell+1,m+1}^*(r)R_{\ell m}(r)$$

$$+ \kappa_\ell^{-m}R_{\ell+1,m-1}^*(r)R_{\ell m}(r)\big]. \quad \text{(A6)}$$

[1] D. Shafir, Y. Mairesse, D. M. Villeneuve, P. B. Corkum, and N. Dudovich, Nat. Phys. **5**, 412 (2009).

[2] D. Shafir, H. Soifer, B. D. Bruner, M. Dagan, Y. Mairesse, S. Patchkovskii, M. Y. Ivanov, O. Smirnova, and N. Dudovich, Nature (London) **485**, 343 (2012).

[3] L. Zhang, X. Xie, S. Roither, D. Kartashov, Y. L. Wang, C. L. Wang, M. Schöffler, D. Shafir, P. B. Corkum, A. Baltuška, I. Ivanov, A. Kheifets, X. J. Liu, A. Staudte, and M. Kitzler, Phys. Rev. A **90**, 061401(R) (2014).

[4] M. Han, P. Ge, Y. Shao, M.-M. Liu, Y. Deng, C. Wu, Q. Gong, and Y. Liu, Phys. Rev. Lett. **119**, 073201 (2017).

[5] M. Li, H. Xie, W. Cao, S. Luo, J. Tan, Y. Feng, B. Du, W. Zhang, Y. Li, Q. Zhang, P. Lan, Y. Zhou, and P. Lu, Phys. Rev. Lett. **122**, 183202 (2019).

[6] M. Kitzler and M. Lezius, Phys. Rev. Lett. **95**, 253001 (2005).

[7] M. Kitzler, X. Xie, A. Scrinzi, and A. Baltuska, Phys. Rev. A **76**, 011801(R) (2007).

[8] D. B. Milošević and W. Becker, Phys. Rev. A **100**, 031401(R) (2019).

[9] J. Heslar, D. Telnov, and S.-I. Chu, Phys. Rev. A **83**, 043414 (2011).

[10] H. Eichmann, A. Egbert, S. Nolte, C. Momma, B. Wellegehausen, W. Becker, S. Long, and J. K. McIver, Phys. Rev. A **51**, R3414 (1995).

[11] M. Richter, M. Kunitski, M. Schöffler, T. Jahnke, L. P. H. Schmidt, M. Li, Y. Liu, and R. Dörner, Phys. Rev. Lett. **114**, 143001 (2015).

[12] X. Xie, T. Wang, S. G. Yu, X. Y. Lai, S. Roither, D. Kartashov, A. Baltuška, X. J. Liu, A. Staudte, and M. Kitzler, Phys. Rev. Lett. **119**, 243201 (2017).

[13] M. Murakami, G. P. Zhang, and S.-I. Chu, Phys. Rev. A **95**, 053419 (2017).

[14] C. A. Ullrich, U. J. Gossmann, and E. K. U. Gross, Phys. Rev. Lett. **74**, 872 (1995).

[15] L. Brugnera, D. J. Hoffmann, T. Siegel, F. Frank, A. Zaïr, J. W. G. Tisch, and J. P. Marangos, Phys. Rev. Lett. **107**, 153902 (2011).

[16] C. P. J. Martiny, M. Abu-samha, and L. B. Madsen, J. Phys. B: At., Mol., Opt. Phys. **42**, 161001 (2009).

[17] J. Zhao and M. Lein, Phys. Rev. Lett. **111**, 043901 (2013).

[18] M. Murakami, O. Korobkin, and M. Horbatsch, Phys. Rev. A **88**, 063419 (2013).

[19] I. A. Ivanov and A. S. Kheifets, Phys. Rev. A **89**, 021402(R) (2014).

[20] J.-W. Geng, L. Qin, M. Li, W.-H. Xiong, Y. Liu, Q. Gong, and L.-Y. Peng, J. Phys. B: At., Mol., Opt. Phys. **47**, 204027 (2014).

[21] J. Kaushal and O. Smirnova, Phys. Rev. A **88**, 013421 (2013).

[22] J.-W. Geng, W.-H. Xiong, X.-R. Xiao, L.-Y. Peng, and Q. Gong, Phys. Rev. Lett. **115**, 193001 (2015).

[23] D. Shafir, Y. Mairesse, H. J. Wörner, K. Rupnik, D. M. Villeneuve, P. B. Corkum, and N. Dudovich, New J. Phys. **12**, 073032 (2010).

[24] R. D. Cowan, *The Theory of Atomic Structure and Spectra* (University of California Press, Oakland, CA, 1981).

[25] X.-M. Tong and S.-I. Chu, Chem. Phys. **217**, 119 (1997).

[26] P. Hohenberg and W. Kohn, Phys. Rev. **136**, B864 (1964).

[27] E. Runge and E. K. U. Gross, Phys. Rev. Lett. **52**, 997 (1984).

[28] X.-M. Tong and S.-I. Chu, Phys. Rev. A **55**, 3406 (1997).

[29] J. B. Krieger, Y. Li, and G. J. Iafrate, Phys. Rev. A **45**, 101 (1992).

[30] M. Murakami, G. P. Zhang, D. A. Telnov, and S.-I. Chu, J. Phys. B: At., Mol., Opt. Phys. **51**, 175002 (2018).

[31] X.-M. Tong and S.-I. Chu, Phys. Rev. A **57**, 452 (1998).

[32] N. Schaeffer, Geochem., Geophys., Geosyst. **14**, 751 (2013).

[33] V. V. Strelkov, M. A. Khokhlova, A. A. Gonoskov, I. A. Gonoskov, and M. Y. Ryabikin, Phys. Rev. A **86**, 013404 (2012).

[34] G. Vignale, Phys. Rev. Lett. **74**, 3233 (1995).

[35] C. C. Chiril, I. Dreissigacker, E. V. van der Zwan, and M. Lein, Phys. Rev. A **81**, 033412 (2010).

[36] P. B. Corkum, Phys. Rev. Lett. **71**, 1994 (1993).

[37] M. Lewenstein, P. Balcou, M. Y. Ivanov, A. L'Huillier, and P. B. Corkum, Phys. Rev. A **49**, 2117 (1994).

[38] M. B. Gaarde, P. Antoine, A. L'Huillier, K. J. Schafer, and K. C. Kulander, Phys. Rev. A **57**, 4553 (1998).

[39] B. Zhang and M. Lein, Phys. Rev. A **100**, 043401 (2019).

[40] L. D. Landau and E. M. Lifshitz, *Quantum Mechanics; Non-relativistic Theory*, 2nd ed. (Butterworth-Heinemann, London, 1981), Chap. 29.